

Accepted Manuscript

Synthesis and characterization of diphenylamine derivative containing malononitrile for thermally activated delayed fluorescent emitter

Sunyoung Sohn, Bong Hyun Koh, Jae Yeul Baek, Hyun Chan Byun, Jae Hyun Lee, Dong-Seon Shin, Hyungju Ahn, Han-Koo Lee, Jaeyoung Hwang, Sungjune Jung, Yun-Hi Kim

PII: S0143-7208(16)31223-2

DOI: [10.1016/j.dyepig.2017.01.010](https://doi.org/10.1016/j.dyepig.2017.01.010)

Reference: DYPI 5709

To appear in: *Dyes and Pigments*

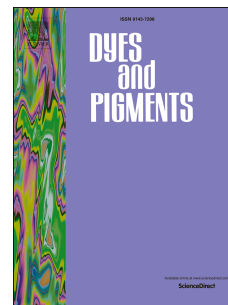
Received Date: 18 November 2016

Revised Date: 17 December 2016

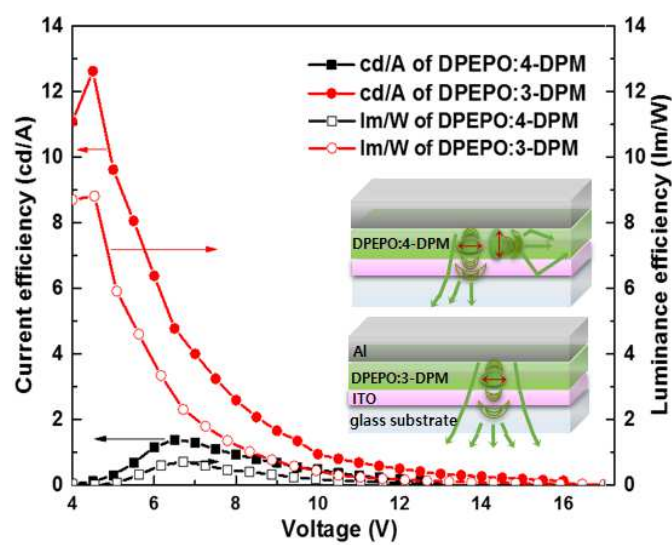
Accepted Date: 6 January 2017

Please cite this article as: Sohn S, Hyun Koh B, Baek JY, Chan Byun H, Lee JH, Shin D-S, Ahn H, Lee H-K, Hwang J, Jung S, Kim Y-H, Synthesis and characterization of diphenylamine derivative containing malononitrile for thermally activated delayed fluorescent emitter, *Dyes and Pigments* (2017), doi: [10.1016/j.dyepig.2017.01.010](https://doi.org/10.1016/j.dyepig.2017.01.010).

This is a PDF file of an unedited manuscript that has been accepted for publication. As a service to our customers we are providing this early version of the manuscript. The manuscript will undergo copyediting, typesetting, and review of the resulting proof before it is published in its final form. Please note that during the production process errors may be discovered which could affect the content, and all legal disclaimers that apply to the journal pertain.



Graphical abstract



Synthesis and characterization of diphenylamine derivative containing malononitrile for thermally activated delayed fluorescent emitter

Sunyoung Sohn ^{a,1}, Bong Hyun Koh ^{b,1}, Jae Yeul Baek ^b, Hyun Chan Byun ^b, Jae Hyun Lee ^b,
Dong-Seon Shin ^b, Hyungju Ahn ^c, Han-Koo Lee ^c, Jaeyoung Hwang ^d, Sungjune Jung ^{a,**},
Yun-Hi Kim ^{d,*}

^a *Department of Creative IT Engineering, Pohang University of Science and Technology, Pohang 37673, Republic of Korea*

^b *Kyeong-Nam Science High School, Jinju 52620, Republic of Korea*

^c *Pohang Accelerator Laboratory, Pohang 37673, Republic of Korea*

^d *Department of Chemistry and Research Institute for Green Energy Convergence Technology, Gyeongsang National University, Jinju 52828, Republic of Korea*

To increase the efficiency of blue organic light-emitting diodes (OLEDs), new blue dopants, 2-(bis(4-(diphenylamino)phenyl)methylene)malononitrile (4-DPM) and 2-(bis(3-(diphenylamino)phenyl)methylene)malononitrile (3-DPM), with thermally activated delayed fluorescence were synthesized. 4-DPM with a *p*-phenyl linker between the electron-donating diphenylamine unit and the electron-withdrawing malonitrile unit showed a large overlap in the phenyl linker as well as the malonitrile unit, while 3-DPM with an *m*-phenyl linker showed a weak overlap in the phenyl linker. The OLED with the 3-DPM dopant showed higher efficiencies of 12.62 cd/A and 8.81 lm/W compared to that with the 4-DPM dopant (1.38 cd/A and 0.70 lm/W). This result was attributed to the small overlap between the electron-donating and electron-withdrawing units, the small charge-transfer singlet-triplet state splitting below 0.1 eV, and the well-aligned structure in the horizontal direction, as determined by grazing incidence X-ray diffraction.

Keywords: OLEDs, TADF, GIXD, Horizontal orientation, ΔE_{ST} , Phenyl linker

* Corresponding author. Department of Chemistry and Research Institute for Green Energy Convergence Technology, Gyeongsang National University, Jinju 52828, Republic of Korea.
Tel.: +82-55-772-1491 ; fax: +82-55-772-1489.

** Corresponding author.

E-mail addresses : sjjung@postech.ac.kr (S. Jung), ykim@gnu.ac.kr (Y.-H. Kim).

¹ Both authors contributed equally to this work.

1. Introduction

Organic light-emitting diodes (OLEDs) have been used in flat-panel displays and general light applications because of their many advantages such as self-emission, flexibility, large-area fabrication, low cost, and low power consumption [1,2]. However, the efficiency of first-generation fluorescence-based OLEDs is limited because spin-allowed emission is generated only by singlet (S_1) exciton. In contrast, in second-generation phosphorescent OLEDs (PHOLEDs), exciton harvesting by the triplet (T_1) state via intersystem crossing leads to an internal efficiency of nearly 100%. However, it remains challenging to produce cost-effective and efficient pure-blue OLEDs with long-term stability because of the incorporation of organometallic complexes containing rare and heavy transition metals (such as iridium and platinum), for example, tris(2-phenylpyridinato)iridium(III) [3]. In 2009, thermally activated delayed fluorescence (TADF) materials were proposed as a third-generation material and have since been studied intensively by Adachi et al [4,5]. As compared to PHOLEDs containing rare metal complexes, TADF materials have many advantages such as easy synthesis using pure organic molecules, low driving voltage, and lower triplet and singlet energy levels. In addition, it harvesting both single and triplet excitons because TADF involves small charge-transfer singlet-triplet state splitting (ΔE_{ST}) by thermal activation between the lowest T_1 and lowest excited S_1 states, resulting in fluorescence in S_1 [6-8]. Currently, blue TADF devices show relatively low quantum efficiencies (e.g., 19.5% in 2014 and 22.3% in 2015 with deep blue color, and 25% in 2016 with light blue color) compared to green TADF devices (29.6% in 2014) [7, 9-11]. However, a few studies have achieved high efficiency and good color purity in blue TADF OLEDs. For example, for deep-blue color, the synthesis of a new donor unit of the azasiline group, design of a carbazole donor moiety, and triazine acceptor moiety were developed. For high efficiency, very large dihedral angles, small ΔE_{ST} (<0.1 eV), and molecular design without complex chemical modification, which

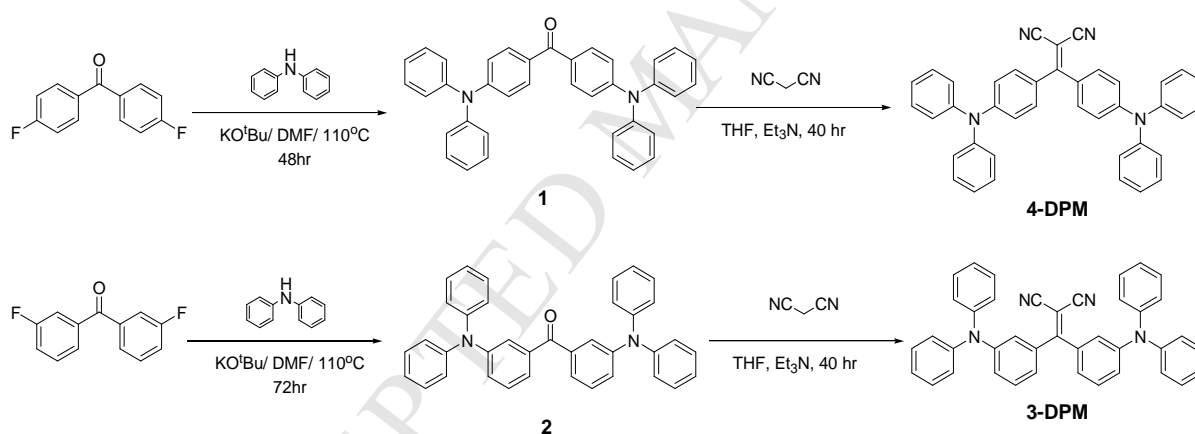
is only substituting into meta positions of the electron-accepting units [5,7,10,12]. Minimizing ΔE_{ST} is the first priority because TADF efficiency depends on the rate of $S_1 \leftarrow T_1$ intersystem crossing as well as a small overlap of the work function of the highest occupied molecular orbital (HOMO, Φ_{HOMO}) and the lowest unoccupied molecular orbital (LUMO, Φ_{LUMO}), which results in a spatial separation between HOMO and LUMO [12].

In addition, the molecular orientation of the emitting material is known as a key to determine OLED efficiency by considering the outcoupling enhancement caused by a reduced coupling to surface plasmons. For example, emitters with perfectly horizontal orientations can increase the external efficiency by up to 46%, which is higher than that achieved by isotropically oriented molecules [13-15]. In 2014, Brutting analyzed the molecular orientations of the transition dipole moments in sky-blue TADF molecules and fluorescent green emitters based on the angular dependent photoluminescence (PL) spectra and the calculated dipole moments of the TADF emitters obtained using variable-angle spectroscopic ellipsometry [13,14]. Kim et al. have been widely studying the molecular orientations in some iridium complexes, and a non-doped, Pt-based emitter by grazing incidence wide-angle X-ray diffraction (GIXD), along with a mixed host consisting of a hole-transporting material and an electron-transporting material sky-blue TADF OLEDs by angle dependent PL spectra for sky-blue TADF OLEDs [15,16]. Although the preferred dipole orientation may be one of the most important properties of a TADF emitter, two-dimensional GIXD (2D-GIXD) analysis using scattered X-rays has not been used to clarify the molecular orientations. In this study, we synthesized new TADF blue dopants, 2-(bis(4-(diphenylamino)phenyl)methylene) malononitrile (4-DPM) with a *p*-phenyl linker and 2-(bis(3-(diphenylamino)phenyl)methylene)malononitrile (3-DPM) with an *m*-phenyl linker between an electron-donating diphenylamine unit and an electron-withdrawing malonitrile unit. Furthermore, we focused on the effect of molecular orientations (para and meta

positions) of the substituent phenyl linkers on the device efficiency using 2D-GIXD analysis, because the functional linker position leads to harvesting of both singlet and triplet excitons, which in turn affects the device properties. In addition, we analyzed the scattered X-ray intensities of the host and host:dopant films along with the spectra of in-plane and out-of-plane scattering to the plane and azimuthal intensity profiles for a plot of orientation distribution. To the best of our knowledge, this is the first study on molecular orientation using 2D-GIXD analysis in blue TADF emitters, and the results will contribute to basic research on TADF molecular design.

2. Experiments

2.1. Synthesis of materials



Scheme 1. Synthetic route of compounds 4-DPM and 3-DPM.

2.1.1 Synthesis of bis(4-(diphenylamino)phenyl)methanone

Diphenylamine (3.4 g, 20 mmol) and KOtBu (3.37 g, 30 mmol) were dissolved in 100 mL anhydrous N,N-dimethylformamide (DMF). Bis(3-fluorophenyl)methanone (2.18 g, 10 mmol) was slowly dropped into 30 mL anhydrous DMF solution. The reaction mixture was refluxed for 48 h at 110 °C under N₂ atmosphere. After cooling to room temperature, water was added and the mixture was extracted with CH₂Cl₂. The combined extract was dried over

anhydrous MgSO_4 and filtered. The solvent was removed by rotary evaporation, and the residue was purified by column chromatography over silica gel with hexane-EtOAc (4:1) as the eluent to yield 4-DPM as a yellow solid (2.3 g, 44.5%). ^1H NMR (300 MHz, CDCl_3), δ (ppm): 7.51 (m, 4H), 7.35 (m, 8H), 7.20 (m, 8H), 7.16 (m, 4H), 7.05 (d, $J = 8.6$ Hz), ^{13}C NMR (75 MHz, CDCl_3), δ (ppm): 192.83, 151.20, 146.37, 131.24, 130.51, 129.15, 125.47, 124.11, 119.70.

2.1.2. Synthesis of 4-DPM

Bis(4-(diphenylamino)phenyl)methanone (1.8 g, 3.48 mmol) and malononitrile (0.33 mL, 5.23 mmol) were dissolved in anhydrous THF (30 mL). Next, four drops of triethylamine were added and the solution was stirred at room temperature for 40 h. The solvent was removed by rotary evaporation, and the residue was purified by column chromatography over silica gel with CH_2Cl_2 /petroleum ether (1:1) as the eluent to yield 4-DPM as a yellow solid (0.52 g, 21%). IR (KBr) ν (cm^{-1}) 2225 (-CN), ^1H NMR (300 MHz, CD_2Cl_2), δ (ppm): 7.71 (d, $J = 8.0$ Hz, 4H), 7.33 (m, 8H), 7.15 (m, 12H), 7.03 (d, $J = 7.8$ Hz, 4H), ^{13}C NMR (75 MHz, CD_2Cl_2), δ (ppm): 192.82, 152.37, 146.45, 131.82, 130.37, 130.04, 126.31, 125.34, 119.13, MS (EI): m/z (%) 564 (100).

2.1.3. Synthesis of bis(3-(diphenylamino)phenyl)methanone

Bis(3-(diphenylamino)phenyl) methanone was obtained as a yellow solid (2.3 g, 44.5 %) using a method similar to that used to prepare bis(4-(diphenylamino)phenyl)methanone. ^1H NMR (300 MHz, CDCl_3): 7.74 (d, $J = 8.0$ Hz, 4H), 7.35 (m, 8H), 7.22(m, 8H), 7.14 (m, 4H), 7.02 (d, $J = 8.0$ Hz, 4H), ^{13}C NMR (75 MHz, CDCl_3): 119.53, 120.38, 123.50, 124.65, 128.69, 129.48, 135.93, 138.20, 147.27, 148.42, 193.23.

2.1.4. Synthesis of 3-DPM

3-DPM was obtained by a method similar to 4-DPM and was obtained as a yellow solid (0.52 g, 21 %). IR (KBr) ν (cm^{-1}) 2223 (-CN), ^1H NMR (300 MHz, CD_2Cl_2), δ (ppm): 7.71 (d, $J = 8.0$ Hz, 4H), 7.33 (m, 8H), 7.15 (m, 12H), 7.03 (d, $J = 7.80$ Hz, 4H), ^{13}C NMR (75 MHz, CD_2Cl_2), δ (ppm): 192.82, 152.37, 146.45, 131.82, 130.37, 130.04, 126.31, 125.34, 119.13, MS (EI): m/z (%) 564 (100).

2.2. Instruments

^1H NMR spectra were recorded using a Bruker Avance-300 MHz FT-NMR spectrometer, and chemical shifts were reported in parts per million with tetramethylsilane as the internal standard. Thermogravimetric analysis (TGA) was performed under nitrogen using a TA instrument 2050 thermogravimetric analyzer. Differential scanning calorimetry (DSC) was conducted under nitrogen using a TA instrument DSC Q10. Samples for both TGA and DSC were heated at a rate of $10\text{ }^\circ\text{C}/\text{min}$. UV-visible spectra were measured using a Shimadzu UV-1065PC UV-visible spectrophotometer. PL spectra were measured using a Perkin Elmer LS50B fluorescence spectrophotometer. The electrochemical properties of the materials were measured by cyclic voltammetry (CV) using an Epsilon C3 in a 0.1 M solution of tetrabutyl ammonium perchlorate in acetonitrile. The topographies of bis[2-(diphenylphosphino)phenyl]ether oxide (DPEPO), DPEPO:4-DPM(10 wt.%), and DPEPO:3-DPM(10 wt.%) films were analyzed using atomic force microscopy (AFM; VEECO Dimension 3100+Nanoscope V) in the non-contact mode. Near-edge X-ray absorption fine structure (NEXAFS) measurements were performed at room temperature at the 4D beamline of the Pohang Light Source (PLS-II) of the Pohang Accelerator Laboratory (PAL). We used the partial-electron-yield detection mode for NEXAFS spectra by recording the sample current normalized to a signal current measured simultaneously using a gold mesh in

ultrahigh vacuum. We used a polarized (*p*-polarized) synchrotron photon beam ($\sim 85\%$) with energy in the range of 279 to 325 eV, a spectral energy resolution of $\Delta E = 150$ meV, and a probing depth of ~ 50 Å for surface-sensitive measurements. Two-dimensional-GIXD measurements were conducted at the PLS-II 9A U-SAXS beamline of PAL. The X-rays coming from the in-vacuum undulator were monochromated (wavelength $\lambda = 1.120$ Å) using a double-crystal monochromator and focused both horizontally and vertically (FWHM $300 \mu\text{m}$ (H) \times 30 (V) μm at sample position) using K-B-type mirrors. The vacuum GIXD system was equipped with a seven-axis-motorized sample stage for a fine alignment of thin films. GIXD patterns were recorded with a 2D CCD detector (Rayonix SX165, USA) under an X-ray irradiation time of 10 s.

2.3. Device fabrication and measurements

OLED devices were fabricated on ITO-coated glass substrates with a structure of ITO/NPB(40 nm)/TcTa(20 nm)/host:dopant(20 nm)/DPEPO(10 nm)/TPBi(30 nm)/Liq(1 nm)/Al (120 nm) in a class-1000 cleanroom. Before use, the ITO-coated glass with a resistance of $15 \Omega/\text{sq}$ was sequentially cleaned with deionized water, acetone, and isopropyl alcohol for 15 min in an ultrasonic bath, and then, treated with O_2 plasma for 60 s. To fabricate the OLEDs, *N,N'*-di(1-naphthyl)-*N,N'*-diphenyl-1,1'-biphenyl-4,4'-diamine (NPB) and tris(4-carbazoyl-9-ylphenyl)amine (TcTa) were used as a hole transport layer and a hole injection layer, respectively. To achieve blue emission, we used an emitting material layer consisting of 10 wt.% 4-DPM and 3-DPM dopants in DPEPO host. DPEPO was also used as an exciton-blocking layer due its high current density, shallow LUMO level, and deep HOMO level for the carrier injection. 1,3,5-tris(*N*-phenylbenzimidazole-2-yl)benzene (TPBi) was used as an electron transport layer, and 8-hydroxyquinolatolithium (Liq) and aluminum

(Al) were thermally evaporated as an interlayer and a cathode, respectively. Current density, luminance, and efficiencies versus driving voltage were measured using the Keithley 236 and CS-1000 (Konica Minolta Co.) system. Transient electroluminescence (EL) curves of devices were measured using a pulsed ND-YAG laser; the wavelength of the excitation source was 355 nm.

3. Results and discussion

3.1. Computational calculation

To predict the optimized geometries and frontier molecular orbital energy levels for 4-DPM and 3-DPM, density functional theory (DFT) calculations are carried out at the B3LYP/6-31G(d) level using Gaussian 09. The HOMO and LUMO distributions of 4-DPM and 3-DPM are shown in Fig 1. The HOMO of 4-DPM, which has a p-phenyl linker between the electron-donating diphenylamine unit and the electron-withdrawing malonitrile unit, is distributed throughout the molecule, while the LUMO is distributed on the malonitrile unit. In 3-DPM, which has an m-phenyl linker, the HOMO is distributed on the diphenylamine unit and the LUMO is distributed on the malonitrile unit. 4-DPM has a large overlap in the phenyl linker and the malonitrile unit, whereas 3-DPM has a weak overlap in the phenyl linker.

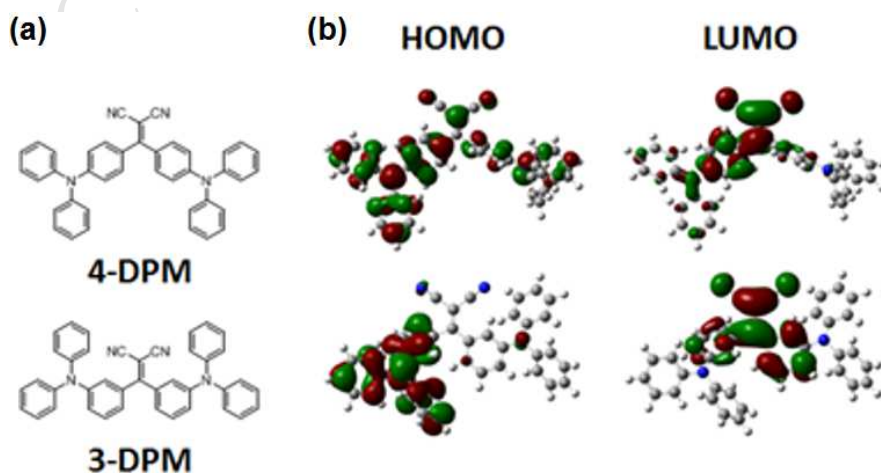


Fig. 1. Results of density functional theory (DFT) calculations of 4-DPM and 3-DPM performed at the B3LYP/6-31G level: (a) chemical structures and (b) HOMO and LUMO electron density maps.

Table 1

HOMO, LUMO, E_g , S_1 , T_1 , and ΔE_{ST} values of 4-DPM, 3-DPM.

	HOMO(eV)	LUMO(eV)	E_g (eV)	S_1 (eV)	T_1 (eV)	ΔE_{ST} (eV)
4-DPM	7.22	5.15	2.07	3.7316	3.6176	0.114
3-DPM	7.27	5.42	1.85	3.7452	3.6472	0.098

We also calculate the energy band gaps (E_g) and the lowest singlet and triplet excited states for the optimized ground-state geometries of 4-DPM and 3-DPM using time-dependent DFT (TD-DFT) calculations with the same functional and basis set. The calculated excited states are used to estimate ΔE_{ST} values of 0.114 and 0.098 eV for 4-DPM and 3-DPM, respectively (Table 1). The TD-DFT calculation provides $\Delta E_{ST} < 0.2$ eV for both compounds.

3.2. Photophysics properties

The absorption and emission spectra of 4-DPM and 3-DPM in cyclohexane, toluene, chloroform, acetone, and DMF solvent are shown in Fig. 2. In all solvents, the PL spectra of 4-DPM and 3-DPM show solvatochromic shifts proportional to solvent-induced polarization.

3.3. Thermal properties

The thermal properties of 4-DPM and 3-DPM are investigated by TGA and DSC. The thermal decomposition temperature (T_d), defined as the temperature at which 5% mass loss occurs, is determined from the TGA results. As shown in Fig. 3, the T_d values of 4-DPM and

3-DPM are 376 °C and 359 °C, respectively. The glass transition temperature (T_g) values of both 4-DPM and 3-DPM are 189 °C.

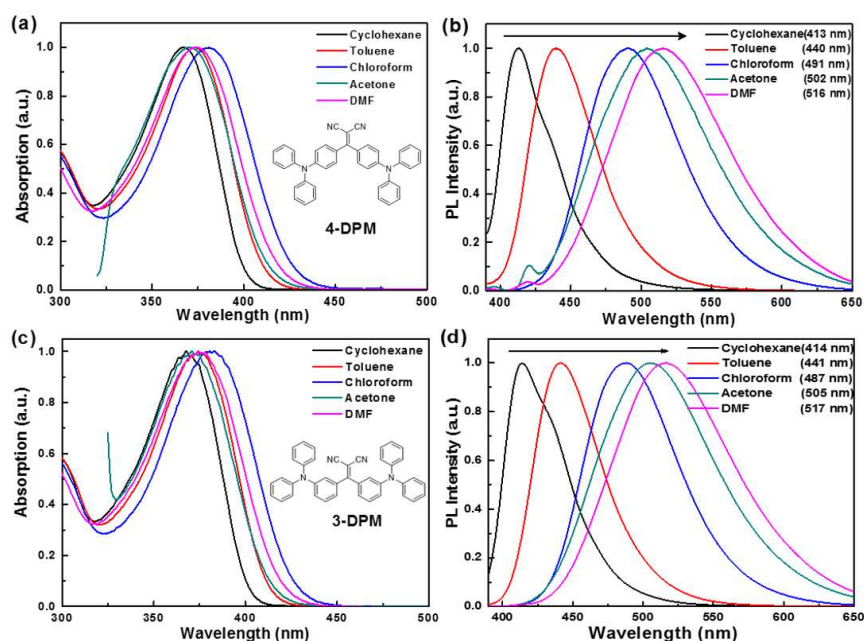


Fig. 2. Absorption and PL spectra of (a), (b) 4-DPM and (c), (d) 3-DPM in solvents with different polarities.

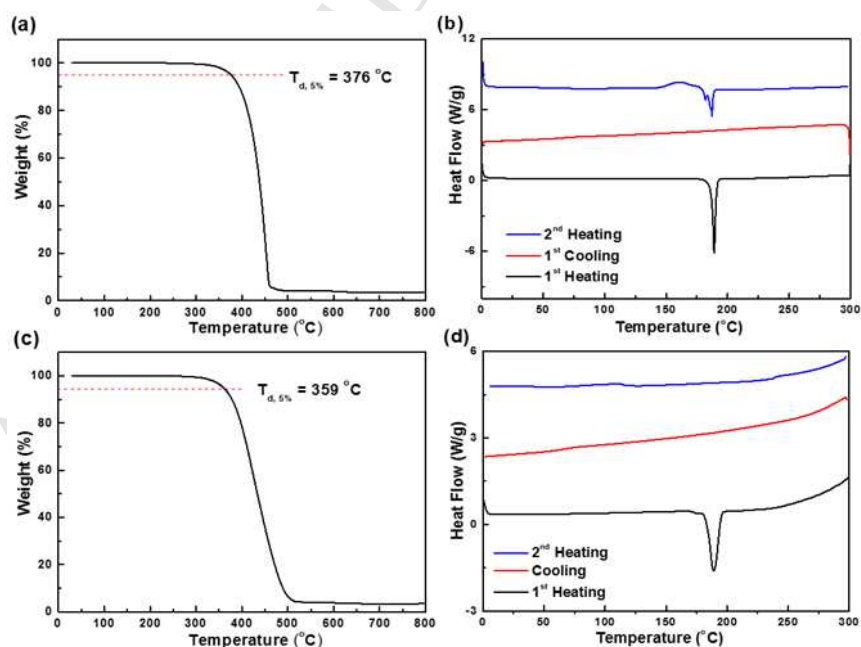


Fig. 3. Thermogravimetric analysis (TGA) and differential scanning calorimetry (DSC) curves of (a), (b) 4-DPM and (c), (d) 3-DPM.

3.4. Electrochemical analysis

The electrochemical properties of 4-DPM and 3-DPM are studied in CHCl_3 solution using CV with ferrocene as the internal standard. The HOMO and LUMO energy levels of both compounds are estimated according to the electrochemical performance and the UV-Vis absorption spectra. The E_g of 4-DPM and 3-DPM, estimated from the long-wavelength absorption edges in CHCl_3 solvent, are 2.92 and 2.91 eV, and the HOMO energy levels are estimated to be -5.18 and -5.21 eV, respectively (Fig. 4). From the equation $E_{\text{LUMO}} = E_{\text{HOMO}} + E_g$, the LUMO energy levels of 4-DPM and 3-DPM are determined to be -2.26 and -2.30 eV, respectively.

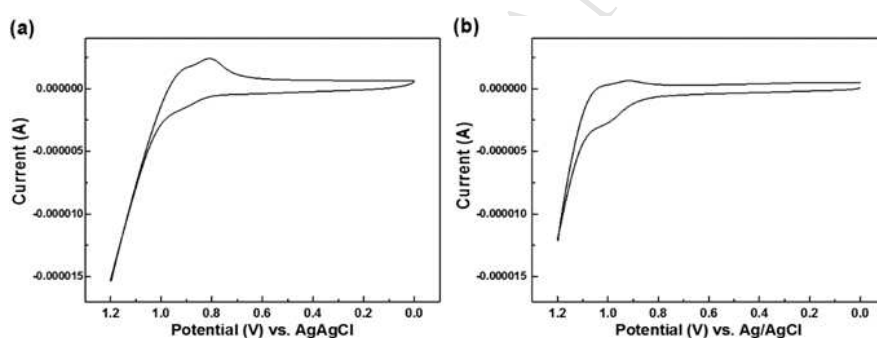


Fig. 4. Cyclic voltammetry (CV) measurements of (a) 4-DPM and (b) 3-DPM dissolved in acetonitrile with 0.1 M $n\text{-Bu}_4\text{NClO}_4$. Working electrode: glassy carbon, scan rate: 100 mVs^{-1} .

3.5. General physical properties

The topographical 2D and 3D images of DPEPO, DPEPO:4-DPM, and DPEPO:3-DPM films with thicknesses of 50 nm are measured by AFM (scan size = $5 \mu\text{m} \times 5 \mu\text{m}$; see Fig. 5). The R_q values corresponding to root-mean-square (rms) averages of the height deviations of the DPEPO, DPEPO:4-DPM(10 wt.%), and DPEPO:3-DPM(10 wt.%) films are 0.33, 0.56, and 0.46 nm, respectively. The surfaces of all films are sufficiently uniform to fabricate

TADF-OLEDs with low leakage current [15]. However, the DPEPO:4-DPM film shows non-uniformly dispersed surface with partially nanocrystals (width = 0.9 nm, height = 0.6 nm) compared to those of the DPEPO film (width = 0.3 nm, height = 0.19 nm) and DPEPO:3-DPM film (width = 0.6 nm, height = 0.3 nm). This may be because the DPEPO:4-DPM film has a relatively rough surface morphology and non-uniformly stacked molecules due to random orientation.

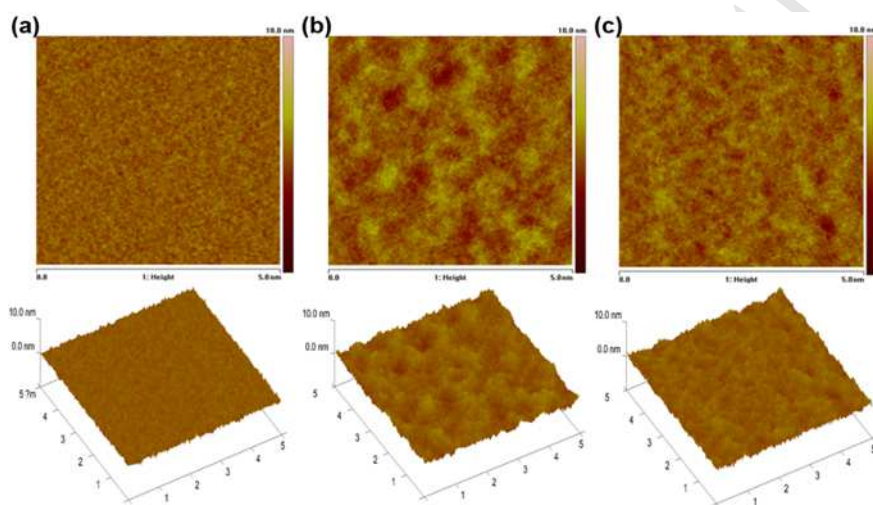


Fig. 5. Two-dimensional and 3D topographical AFM images of (a) DPEPO, (b) DPEPO:4-DPM, and (c) DPEPO:3-DPM films at 5 μm scan size.

The features in the NEXAFS spectra (Supplementary Fig. S1) acquired from the DPEPO:4-DPM and DPEPO:3-DPM films are assigned as the π^* (C=C) orbital at 284.5 eV, the σ^* (C-H) orbital mixed with Rydberg orbitals around 287 to 291 eV, and several σ^* orbitals in the energy range of 292 to 307 eV. We attempt to determine the tilt angle α between the C=C double bond in the conjugated planes and the substrate surface with a photon beam size of approximately $0.1 \times 0.3 \text{ nm}^2$. From the best fit in the inset, we obtain an ensemble average tilt angle of approximately $55^\circ \pm 5^\circ$. The peak intensity of the π^* resonance of the DPEPO, DPEPO:4-DPM, and DPEPO:3-DPM films does not change with increasing

incidence angle (θ), and the changes in crystallinity of all films after C=C/C-H change are insignificant. This may be because all films have broad orientation distributions.

To clarify the molecular orientations as a function of substituent positions of a phenyl linker in TADF-OLED characteristics, we analyze the scattered X-ray intensity in the 2D-GIXD patterns of DPEPO, DPEPO:4-DPM, and DPEPO:3-DPM films with the spectra of scattering in-plane and out-of-plane to the plane and azimuthal angle scan (see Fig. 6). In the 2D-GIXD patterns, q_{xy} and q_z represent the in-plane and out-of-plane components of the scattering vector q , which are normal to the plane of incidence and the sample surface plane, respectively. The azimuthal intensity profiles are plots of orientation distribution. The 2D-GIXD patterns reveal the crystallinities of DPEPO, DPEPO:4-DPM, and DPEPO:3-DPM on the substrate. As shown in Figs. 6(a), (b), and (c), pristine DPEPO, DPEPO:4-DPM, and DPEPO:3-DPM show intensified out-of-plane reflections at $q_{r,z} = 0.706 \text{ \AA}^{-1}$ and 1.406 \AA^{-1} , corresponding to the (100) and (200) reflections of DPEPO. The (100) layer distance of DPEPO ($= 2\pi/q^*$) is 8.9 \AA . In case of DPEPO:4-DPM, additional reflections [highlighted by red circles in Fig. 6(b)] are also observed along the out-of-plane direction at the surface ($\alpha_i=0.08$) in Fig. 6(e). The multiple reflections observed at the surface are induced by the aggregation and self-crystallization of the 4-DPM dopant at the surface. This result is consistent with the surface morphology of DPEPO:4-DPM shown in Fig. 5(b). The inner structures and out-of-plane intensity profiles for the surfaces of pristine DPEPO, DPEPO:4-DPM, and DPEPO:3-DPM are shown in Figs. 6(d) ($\alpha_i=0.12^\circ$) and (e) ($\alpha_i=0.08^\circ$). As shown in the intensity profiles, the (100) and (200) reflections of DPEPO are observed at the surfaces and inner structures. However, multiple reflections for 4-DPM aggregates (red solid arrows) are only observed at the surface, indicating that 4-DPM aggregates are mainly distributed at the film surface. Moreover, the peak intensity and width of the (100) reflection of DPEPO:4-DPM are significantly weakened and broadened. These results imply that the crystallinity of

DPEPO:4-DPM is weaker than that of pristine DPEPO and DPEPO:3-DPM because the aggregated 4-DPM interrupts the crystallization of DPEPO.

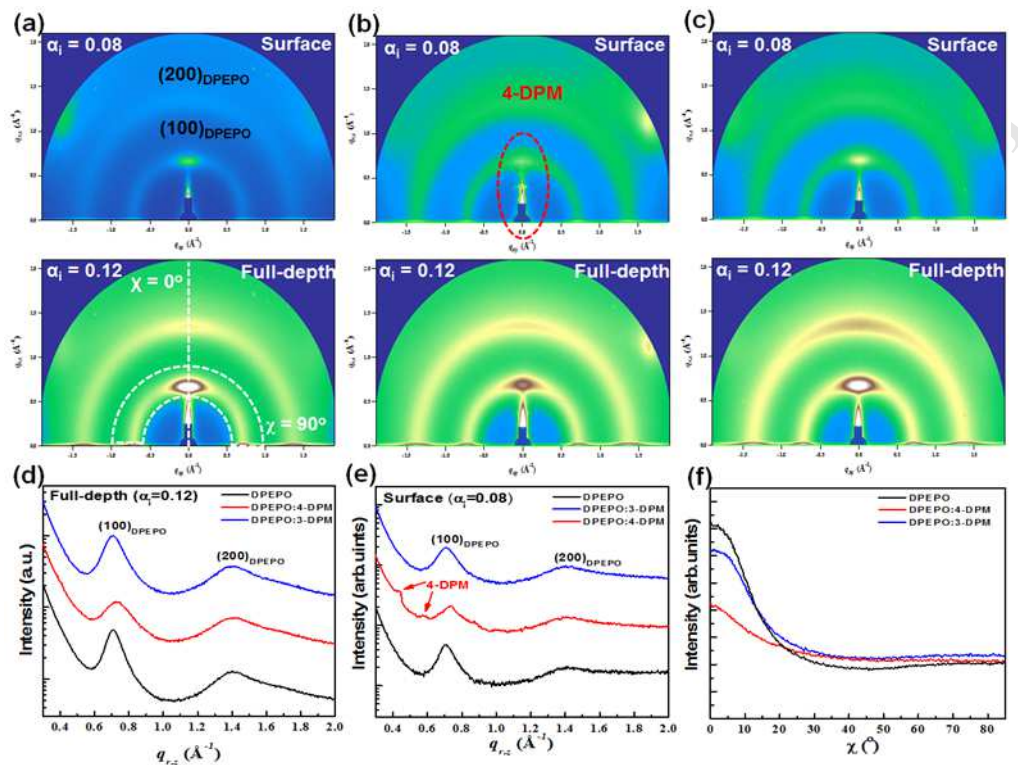


Fig. 6. Two-dimensional GIXD images of scattered X-ray intensity from surface to full depth for (a) DPEPO, (b) DPEPO:4-DPM, and (c) DPEPO:3-DPM films on SiO₂/Si substrates. The vertical and horizontal axes correspond to in-plane and out-of-plane scattering to the plane of the films, whose spectra are, respectively, shown in (d) and (e). (f) Azimuthal intensity plotting the orientation distributions of particular sets of crystallographic reciprocal lattice planes of the films.

To elucidate the crystalline orientation of DPEPO, the azimuthal angle scans of (100) reflection are shown in Fig. 6(f). The azimuthal intensity profiles allow the study of the orientational distribution of the reflections as a function of all possible crystalline orientations [15]. The angular volume fractions of the films show that all films adopt a preferential

horizontal orientation in the emission layer since the maximum intensities are observed at about $\chi=0^\circ$. In particular, most of the crystallinity in the pristine DPEPO film is preferentially horizontal plane-on orientation within the FWHM of 23° , while the crystallinity of 3-DPM is a relatively narrow distribution within the FWHM of 25° compared with that of DPEPO:4-DPM; that the crystallinity of DPEPO:4-DPM is more randomly distributed and exhibits low crystallinity within the FWHM of 28° compare to DPEPO and DPEPO:3-DPM.

3.6. Device characteristics

As the evidence of the contribution of TADF triplet excitations, we conduct time-resolved EL measurements on the microsecond timescale (Supplementary Fig. S2). Two TADF devices with DPEPO:4-DPM and DPEPO:3-DPM emitters show delayed fluorescence and have similar values of about $10 \mu\text{s}$, as shown in inset. It is because of the similar ΔE_{ST} values of 0.114 and 0.098 eV for 4-DPM and 3-DPM, respectively. The current density of TADF-OLEDs with the 4-DPM and 3-DPM show similar property (Supplementary Fig. S3). In contrast, the current efficiency of TADF-OLED with the 3-DPM dopant (12.62 cd/A) is approximately 9.1 times higher than that of the device with the 4-DPM dopant (1.38 cd/A), and its luminance efficiency is 12.5 times greater (8.81 vs. 0.70 lm/W); the CIE coordinates of the 3-DPM and 4-DPM devices are (0.16, 0.20) and (0.17, 0.17), respectively (Fig. 7(a)). The enhanced efficiency of the DPEPO:3-DPM device results from the following two reasons. First is because of the increased internal quantum efficiency by up-converted triplet excitations to the singlet state due to a small overlap between the electron-donating and electron-withdrawing units, as well as a small charge-transfer with ΔE_{ST} below 0.1 eV, as shown in Fig. 1 and Table 1. Second is because of the external quantum efficiency with the light outcoupling effect by the horizontal orientation of the transition dipole moments. The molecular orientation of the DPEPO:3-DPM is similar to that of DPEPO (*i.e.*, horizontal

plane-on molecular alignment), whereas the DPEPO:4-DPM shows weak crystallinity and random orientation of weak horizontal and plane-on orientations (Fig. 6(f)). Thus, the charge transport and light outcoupling of the DPEPO host and 3-DPM dopant are improved due to the well-aligned stacking structure with horizontal orientation compared to the DPEPO:4-DPM with random orientation [13-16].

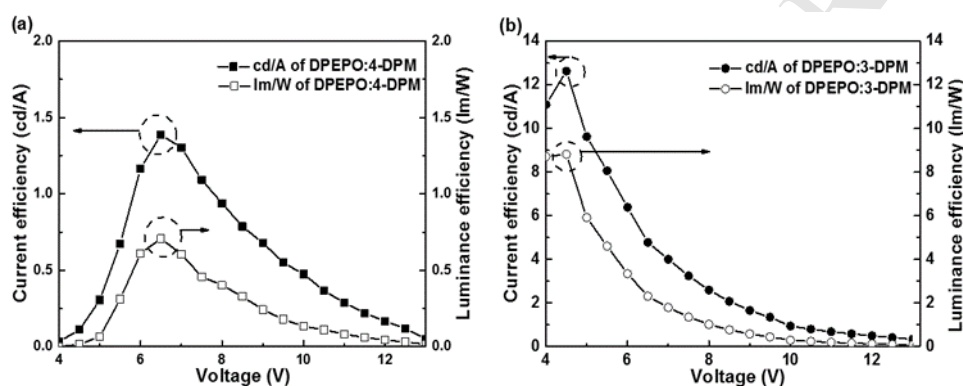


Fig. 7. Current efficiency and luminance efficiency versus applied voltage of TADF devices with (a) DPEPO:4-DPM and (b) DPEPO:3-DPM emitters.

4. CONCLUSION

In summary, we synthesized new deep-blue TADF dopants by using dissolved bis(4-(diphenylamino)phenyl)methanone and malonitrile. We observed that the phenyl linker positions between the electron-donating diphenylamine unit and electron-withdrawing malonitrile unit significantly affected device efficiency. 4-DPM with a *p*-phenyl linker showed that the HOMO level was distributed on the whole molecule and the LUMO level was distributed on the malonitrile unit, resulting in a large overlap in the phenyl linker as well as the malonitrile unit. In 3-DPM with an *m*-phenyl linker, the HOMO was distributed on the diphenylamine unit and the LUMO was distributed on the malonitrile unit, resulting in a weak overlap in the phenyl linker. The calculated ΔE_{ST} values for the optimized ground-state

geometries were similar (0.114 and 0.098 eV for 4-DPM and 3-DPM, respectively). In the final analysis, TADF efficiency depended strongly on the molecular orientation as well as the linker positions. The current efficiency of the TADF-OLED with the 3-DPM dopant (12.62 cd/A) was approximately 9.1 times higher than that of the device with the 4-DPM dopant (1.38 cd/A), and its luminance efficiency was 12.5 times greater (8.81 vs. 0.70 lm/W).

Acknowledgments

This research was supported by Basic Science Research Program through the National Research Foundation of Korea (NRF) funded by the Ministry of Science, ICT & Future Planning(2016R1C1B1011745) and by the Ministry of Science, ICT and Planning of South Korea under the “IT Consilience Creative Program” (IITP-2015-R0346-15-1007) supervised by IITP (Institute for Information & Communications Technology Promotion). The work also supported by the NRF(2015R1A2A1A10055620) and R&D program of MOTIE/KEIT(10048317).

References

- [1] Sohn S, Kim MJ, Jung S, Shin TJ, Lee HK, Kim YH. Molecular orientation of a new anthracene derivative for highly-efficient blue fluorescence OLEDs. *Org Elec* 2015;24:234-40.
- [2] Hwang J, Yook K SY, Lee JY, Kim YH. Synthesis and characterization of phenylpyridine derivative containing an imide functional group on an iridium (III) complex for solution-processable orange phosphorescent organic light-emitting diodes. *Dyes and Pigments* 2015;121:73-8.
- [3] Aizawa N, Park IS, Yasuda T. Design of thermally activated delayed fluorescence materials for organic light-emitting diodes. *AAPPS Bulletin* 2016;26:9-19.
- [4] Endo A, Ogasawara M, Takahashi A, Yokoyama D, Kato Y, Adachi C. Thermally activated delayed fluorescence from Sn^{4+} -porphyrin complexes and their application to organic light emitting diodes A novel mechanism for electroluminescence. *Adv Mater* 2009;21:4802-06.
- [5] Zhang Q, Li B, Huang S, Nomura H, Tanaka H, Adachi C. Efficient blue organic light-emitting diodes employing thermally activated delayed fluorescence. *Nature Photonics* 2014;8:326-32.
- [6] Tao Y, Tuan K, Chen T, Xu P, Li H, Chen R, Zheng C, Zhang L, Huang W. Thermally activated delayed fluorescence materials towards the breakthrough of organoelectronics. *Adv Mater* 2014;26:7931-58.
- [7] Sun JW, Baek JY, Kim KH, Moon CK, Lee JH, Kwon SK, Kim YH, Kim JJ. Thermally activated delayed fluorescence from azasilene based intramolecular charge-transfer emitter (DTPDDA) and a highly efficient blue light emitting diode. *Chem Mater* 2015;27:6675-81.
- [8] Kim Y-H, Wolf C, Cho H, J. S-H, Lee T-W. Highly efficient, simplified, solution-

processed thermally activated delayed-fluorescence organic light-emitting diodes. *Adv Mater* 2016;28:734-41.

[9] Higuchi T, Nakanotani H, Adachi C. High-efficiency white organic light-emitting diodes based on a blue thermally activated delayed fluorescent emitter combined with green and red fluorescent emitters. *Adv Mater* 2015;27:2019-23.

[10] Kim M, Jeon SK, Hwang SH, Lee J Y. Stable blue thermally activated delayed fluorescence organic light emitting diodes with three times longer lifetime than phosphorescent organic light emitting diodes. *Adv Mater* 2015;27:2515-20.

[11] Komatsu R, Sasabe H, Seino Y, Nakao K, Kido J. Light-blue thermally activated delayed fluorescent emitters realizing a high external quantum efficiency of 25% and unprecedented low drive voltage in OLEDs. *J. Mater. Chem. C* 2016;4:2274-78.

[12] Shizu K, Sakai Y, Tanaka H, Hirata S, Adachi C, Kaji H. Metal-linking strategy for thermally activated delayed fluorescence emitters with a small singlet-triplet energy gap. *ITE Trans on MTA* 2015;3:108-13.

[13] Mayr C, Lee SY, Schmidt TD, Yasuda T, Adachi C, Brutting W. Efficiency enhancement of organic light emitting diodes incorporating a highly oriented thermally activated delayed fluorescence emitter. *Adv Funct Mater* 2014;24:5232-39.

[14] Mayr C, Schmidt TD, Brutting W. High-efficiency fluorescent organic light-emitting diodes enabled by triplet-triplet annihilation and horizontal emitter orientation. *Appl Phys Lett* 2014;105:183304-1-4.

[15] Kim K-H, Liao J-L, Lee S W, Sim B, Moon C-K, Lee G-H, Kim H J, Chi Y, Kim J-J. Crystal organic light-emitting diodes with perfectly oriented non-doped Pt-

based emitting layer. *Adv Mater* 2016;28:2526-32.

[16] Sun J W, Kim K-H, Moon C-K, Lee J-H, Kim J-J. Highly efficient sky-blue fluorescence organic light emitting diode based on mixed cohost system for thermally activated delayed fluorescence emitter (2CzPN). *Appl Mater Interfaces* 2016;8:9806-10.

ACCEPTED MANUSCRIPT

Highlight

- Synthesized TADF blue dopants with diphenylamine derivative malononitrile.
- High current efficiency of 12.62 cd/A by dopant with *m*-phenyl linker.
- Low current efficiency of 1.38 cd/A by dopant with *p*-phenyl linker.
- Small charge-transfer singlet-triplet state splitting below 0.1 eV.
- Molecular orientations by substituent positions of a phenyl linker.